In-plane nanoelectromechanical resonators based on silicon nanowire piezoresistive detection

2010 Nanotechnology 21 165504

(http://iopscience.iop.org/0957-4484/21/16/165504)

Nanotechnology **21** (2010) 165504 (7pp) doi:10.1088/0957-4484/21/16/165504

In-plane nanoelectromechanical resonators based on silicon nanowire piezoresistive detection

E Mile[1], G Jourdan[1], I Bargatin[1,2,3], S Labarthe[1], C Marcoux[1], P Andreucci[1], S Hentz[1], C Kharrat[1], E Colinet[1] and L Duraffourg[1]

[1] CEA/LETI MINATEC, 17 rue des Martyrs, 38054 Grenoble Cedex 9, France
[2] Condensed Matter Physics 114-36, California Institute of Technology, Pasadena, CA 91125, USA

E-mail: laurent.duraffourg@cea.fr

Received 8 January 2010, in final form 5 March 2010
Published 30 March 2010
Online at stacks.iop.org/Nano/21/165504

Abstract
We report an actuation/detection scheme with a top-down nanoelectromechanical system (NEMS) for frequency shift based sensing applications with outstanding performance. It relies on electrostatic actuation and piezoresistive nanowire gauges for in-plane motion transduction. The process fabrication is fully CMOS (complementary metal–oxide–semiconductor) compatible. The results show a very large dynamic range of more than 100 dB and an unprecedented signal to background ratio of 69 dB providing an improvement of two orders of magnitude in the detection efficiency presented in the state of the art in NEMS fields. Such a dynamic range results from both negligible $1/f$ noise and very low Johnson noise compared to the thermomechanical noise. This simple low power detection scheme paves the way for new class of robust mass resonant sensors.

(Some figures in this article are in colour only in the electronic version)

1. Introduction

NEMS are actively being explored due to their incredible potential for applications such as in ultrasensitive mass [1–4] and force sensing [5]. However, efficient actuation and sensitive detection at the nanoscale remain a challenge. The small displacements of these miniaturized devices induce very low signals which are overwhelmed by parasitic background. A lot of effort has been devoted to developing new transduction and background reduction [6]. A variety of NEMS detection techniques, such as capacitive [3, 7, 8], magnetomotive [9], piezoresistive [10, 11] and field-emission [4, 12] transduction, have been proposed. The magnetomotive approach typically requires large magnetic fields (2–8 T) and is thus not suitable for integrated applications. The field-emission effect detection demands complex instrumentation and its stability in time is still questionable. Moreover, this technique uses bottom-up approach that is hardly compatible with large scale integration (VLSI) process. A piezoresistive detection scheme offers great potential compared to a capacitive one especially for high resonant frequency measurements [10, 13].

Recently, mass resolution down to 7 zg $Hz^{-1/2}$ [1] has been demonstrated using a metallic gauge layer deposited on the top of a cantilever. Another approach [14] consists in using a doped silicon nanowire that produces a second-order piezoresistive effect for large displacements of the nanowire. However to date bottom-up nanowires cannot be fabricated using a VLSI process compatible with a standard CMOS technology.

In this paper, we demonstrate an original technique of highly efficient in-plane motion detection based on suspended p^{++} doped piezoresistive nanowires connected in a symmetric bridge configuration to a resonating lever arm. The differential bridge architecture provides intrinsic signal amplification and background suppression. We show that detection through silicon gauges has a better signal to noise ratio at room temperature than the metallic layer used as the piezoresistive gauge. Although the Johnson noise is higher with semiconductor nanowire gauges (due to their larger resistance), the increase in signal is much larger than the

[3] Present address: Stanford University, Stanford, CA 94305-4070, USA.

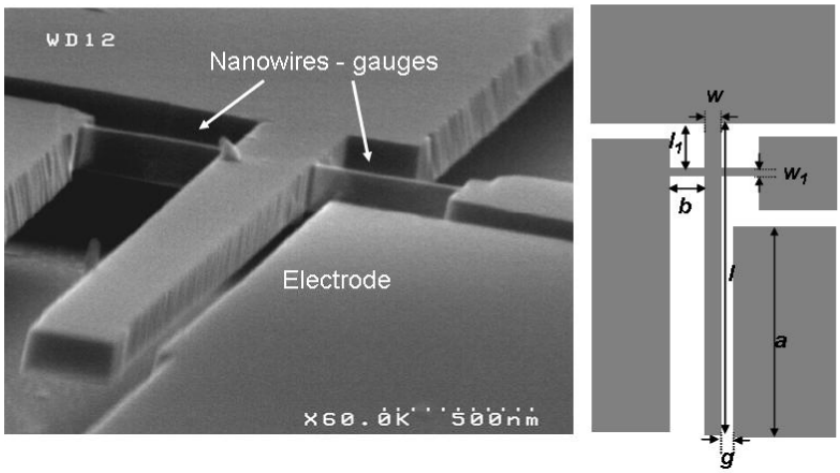

Figure 1. SEM image illustrating the in-plane vibration of the cross beam.

Table 1. Typical values of the device.

Beam length l (μm)	Beam width w (nm)	Anchor/gauge distance l_1 (nm)	Gauge length b (nm)	Gauge width w_1 (nm)	Electrode length a (μm)	Gap electrode/beam g (nm)
5	300	750	500	80	3.5	200

increase in noise. We therefore present an alternative way of using a piezoresistive technique, showing similar performance to the use of metallic gauges. We therefore reconsider the belief that metallic gauges are the best candidates for nanoscale piezoresistive transduction use.

In addition, in-plane motion architecture offers more flexibility of design and simplifies process development. Our device uses CMOS based fabrication and is therefore fully compatible with very large scale integration (VLSI) of NEMS on 200 mm wafer for the future.

This paper starts with an overview of the fabrication process and architecture, continues with measurements and results, and concludes with a discussion of the efficiency of the detection scheme and the frequency stability of these devices.

2. The NEMS resonator and principle of operation

2.1. The device

Advances in top-down lithographic processes have enabled fabrication of nanostructures with sizes similar to those achieved with bottom-up synthesis methods. The NEMS device presented in this paper is fabricated using CMOS compatible materials with nanoelectronic state-of-the-art lithography and etching techniques. It is composed of a fixed–free lever beam and two piezoresistive gauges connected to the cantilever at a distance $l_1 = 0.15l$ from its fixed end where l is the beam length (see table 1). This value was chosen to maximize the stress inside the gauges due to the cantilever motion (see figure 1). The gauges have been etched along the $\langle 110 \rangle$ direction in order to benefit from the high gauge factor associated with p^{++} doped silicon. A drive electrode was patterned along one side of the vibrating beam for electrostatic actuation. The general architecture that looks like a cross beam is given in figure 1 and the device dimensions are summed up in table 1.

The NEMS is a structure from a 200 mm silicon-on-insulator (SOI) wafer of (100) orientation with a 160 nm thick top silicon structural layer (with resistivity of $\approx$10 Ω cm) and a 400 nm thick sacrificial oxide layer. The top silicon layer was implanted with boron ions (p type) through a thin layer of thermal oxide. Homogeneous doping ($\sim 10^{19}$ cm^{-3}) through the whole thickness of the top silicon was obtained through a specific annealing step (for material reconstruction and doping activation commonly used in CMOS technology), resulting in top layer resistivity of approximately 9 mΩ cm. A hybrid e-beam/DUV lithography technique (allowing 50 nm minimum feature size) was used to define the structure (cantilever and nanowire gauges) and electrode pads, respectively [15]. The top silicon layer was etched by anisotropic reactive ion etching (RIE) to get the suspended cross beam formed by the cantilever and the nanowires. In order to decrease the lead resistances, the interconnecting leads have been made thicker with a 650 nm thick layer of AlSi, a typical metal for the CMOS interconnections process. Finally, the nanoresonators have been released using a vapor HF isotropic etching to remove the sacrificial layer of oxide beneath both the cantilever and the nanowire.

1500 devices per wafer of this design are fabricated with this VLSI process. The functionality of the final devices is checked by measuring both the lead and gauge resistances and resonant frequency. The yield is 95% per wafer on average.

The lead resistance of approximately 4 kΩ and the gauge resistance of 3.6 kΩ were measured using the three-point local AFM technique [16].

Table 2. Comparison of predictions of analytical and FEM models—M_{eff} is the effective mass.

	$\omega_0/2\pi$ (MHz)	α	M_{eff}
Analytical model	21.10	6.05	140 fg
FEM model	20.65	5.2	NA

2.2. The principle of operation

As shown in figure 1, two suspended nanowires are structured on each side of the cantilever that works as a lever arm. It is actuated by an electrostatic force at its first eigenfrequency. To evaluate the dynamical behavior we used a model based on Euler–Bernoulli beam theory that is detailed in [13]. From this model, we can easily compute the first eigenfrequency, ω_0, as well as the force F_g acting on the gauges,

$$F_g(\omega) = \alpha \frac{\omega_0^2}{\omega_0^2 - \omega^2 + j\omega\omega_0/Q} F_{el}(\omega), \tag{1}$$

where α, ω, Q and $F_{el}(\omega)$ are the amplification factor of the lever arm, the angular frequency (rad s^{-1}), the quality factor, and the electrostatic driving force respectively.

The electrostatic driving force along the lever beam is given by $F_{el} = 1/2C'V^2$, where V the applied voltage and C' is the derivative of the capacitance C between the cantilever and the drive electrode with respect to the lateral displacement. At resonance, $\omega = \omega_0$ and the force amplification is given by

$$F_g(\omega_0)/F_{el}(\omega_0) = -j\alpha Q. \tag{2}$$

A comparison with the results of finite element modeling (FEM) validated our analytical model to a large extent, as shown in table 2.

The slight discrepancies are due to the assumption that there is no bending moment introduced by the gauges with a perfect anchor.

This design results in a first-order piezoresistive effect (as opposed to a weaker second-order one like in [9]) with the suspended gauges acting as collectors of the stress F_g/s, where s is the cross section area of the gauges. The strain induced in the gauges is transduced into a resistance variation ΔR through the piezoresistive effect:

$$\frac{\Delta R(\omega)}{R} = \gamma\varepsilon(\omega) = \gamma\frac{F_g(\omega)}{2sE} \tag{3}$$

where γ and E are the gauge factor and the Young's modulus of the gauges, respectively. The piezoresistive factor γ is usually written as

$$\gamma = (1 + \nu) + \frac{1}{\varepsilon}\frac{\Delta\rho}{\rho} \tag{4}$$

where ρ, ε and ν are the resistivity, the strain and the Poisson ratio respectively. The gauge factor, which links the mechanical strain in a gauge to its relative resistance change, is caused by two effects. The first is a purely geometric effect and is associated with elastic deformation (the first term in parentheses in equation (4)), while the second corresponds to the modification of the energy bands inside the semiconductor, which alters its resistivity (the second term in equation (4)). For metals, only the first term is significant, and the gauge factor ranges from 1 to 4. For semiconductors, the second term is the most significant contribution. For the chosen ⟨110⟩ crystalline orientation and the doping level of 10^{19} cm^{-3}, the theoretical value is 47 [17]. In our case, γ is evaluated to be around 40 from the amplitude peak at resonance using equations (1) and (2). This experimental result is in good agreement with the theory. Values of material parameters used in this paper are summed up in table 3.

Table 3. Parameters of the cross beam NEMS.

Parameters	E (GPa)	υ	μ (g cm^{-3})	ρ (mΩ cm)	γ
	169	0.26	2330	1.4	40

The device under test was connected to a radio frequency (RF) circuit board through wire bonding and loaded into an RF vacuum chamber for room temperature measurements. At high frequencies, the electrical readout is complicated by parasitic capacitances which change the expected behavior of the electrical circuit. Given the cable capacitance (100 pF m^{-1}), the input impedance of the Stanford Research 830 lock-in amplifier ($R = 10$ MΩ, $C = 25$ pF), and the device pads, the overall parasitic capacitance at the NEMS output is close to $C_p = 125$ pF. This capacitance combines with the electrical resistance of the setup to produce a low pass filter on the output signal with a cut-off frequency of 120 kHz. To avoid parasitic impedances and cross talk, we used a 2ω down-mixing technique to read out the resistance variation at a lower frequency $\Delta\omega$ (typically between 10 and 30 kHz) [18]. A schematic of the setup is shown in figure 2. The cross beam is actuated with a drive voltage V_d at $\omega/2$. Because the electrostatic force is proportional to V_d^2, the strain in the gauges varies at the frequency ω. This technique results in efficient frequency decoupling of the down-mixed signal from parasitic feedthrough. The down-mixed signal read out at the middle of the bridge is proportional to

$$V_{out}(\Delta\omega) \propto \Delta R\cos(\omega t) I_b \cos((\omega + \Delta\omega)t) \sim \tfrac{1}{2} I_b \Delta R \cos(\Delta\omega t) \tag{5}$$

where I_b is the bias current through the gauges induced by the bias voltage V_{bias} (see figure 2).

The two gauges on each side of the lever arm work under equal and opposite tensile and compressive strains. This balanced bridge configuration suppresses the parasitic feedthrough at the middle point of the bridge.

3. Experimental results

The experiments, performed at room temperature and pressure of less than 1 mTorr, showed a remarkably small and flat background, as shown in figure 3. The measured quality factor was approximately 5000 in vacuum and 200 at atmospheric pressure. Quality factors up to 10 000 were measured. The transduction efficiency is usually characterized by the signal to background ratio (SBR) and the signal to noise ratio (SNR).

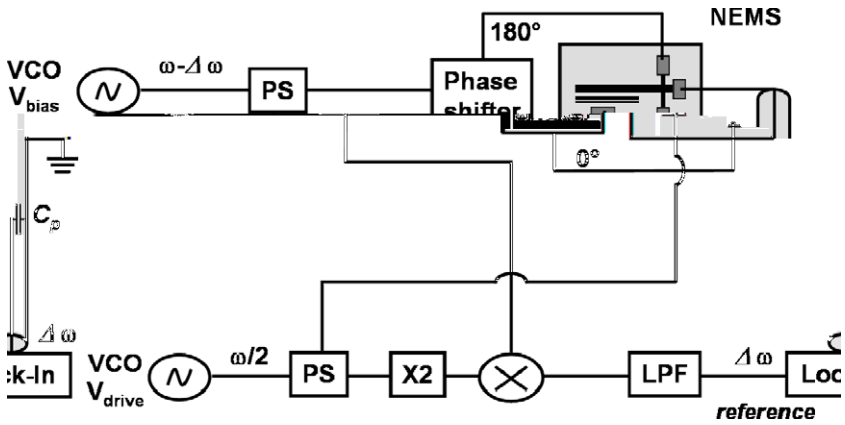

Figure 2. Schematic of the experimental setup used for detecting the resonant motion of the NEMS in figure 1. PS, LPF, VCO, X2 are the power splitter low pass filter, voltage control oscillator and frequency doubler respectively.

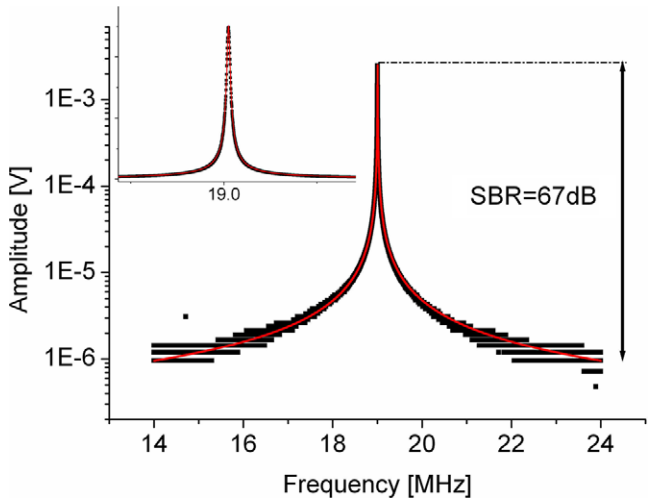

Figure 3. Typical output signal from the structure shown in figure 1 in a vacuum with pressure under 1 mTorr. The signal to background ratio is 67 dB for $V_{\text{drive}} = 1.5$ V and $V_{\text{bias}} = 1.5$ V—sampling time = 30 ms. The inset shows the same data using a linear scale. The maximum voltage (3 mV) corresponds to a displacement of the cantilever end of 10 nm (still largely below the nonlinear regime).

The SBR is the ratio between the useful signal and the background that comes from coupling between the NEMS and the environment. For instance, parasitic capacitance could couple the driving signal with the output. Any noise or drift of these external elements would also be additional noise sources that superimpose on the NEMS noises. The SNR is the ratio between the useful signal and the random variations at the resonance frequency. The resolution is directly deduced from the SNR considering the measurement bandwidth.

3.1. The signal to background ratio

The geometrical and frequency decoupling between the actuation and detection results in a very large signal to background ratio (SBR) of 67 dB. For ultra-low mass sensing, SBR is an important parameter that should be maximized. At the resonance, a large SBR means large variation of the phase for a small frequency shift (Bode representation). In a closed loop (a phase locked loop for instance) the digital error on the readout of the phase will then be low with devices having a large SBR. Furthermore a device with large background will be more sensitive to the random perturbations of its environment. This value is close to two orders of magnitude larger than previous SBR [3, 19, 20] at ambient temperature (300 K). Four reasons for this large SBR can be mentioned. First actuation and detection are well decoupled because they are based on two different techniques. The intrinsic bridge configuration removes the background and improves the SBR by a factor of 5 at least. The lever arm is a cantilever and the nonlinear regime is reached only for large displacements around 100 nm (compared to a double-clamped beam). The electrical actuation can then be quite large around 1.5 V. Finally, the down-mixing techniques that do not depend on the NEMS also improve the SBR by decreasing the background.

The average value per wafer of the resonant frequency is 19.16 MHz with a maximum dispersion of 2%, showing the fairly good reproducibility of the VLSI process.

V_{drive} can be set between a few hundred millivolts and 5 V before having nonlinear behavior of the cantilever. V_{bias} can be set up to 10 V before gauge melting. In the experiment, the voltages are set to a value of 1.5 V, which corresponds to the maximum supplied by our AC generator.

3.2. Noise and the signal to noise ratio

For frequency shift based sensing applications, frequency fluctuations naturally impose a limit on the sensitivity. One source of frequency fluctuations is the finite signal to noise ratio (SNR) at resonance, and the resolution can be defined with the approach presented in [6]. As shown in figure 4, a large SNR of around 100 dB can be obtained with our device. This value is larger than data reported previously (see [1, 10] for example). To measure the noise, we followed the technique described in [18]. There was no external drive, and only a bias voltage was applied to the gauges. The noise (V $\text{Hz}^{-1/2}$) was then measured by sweeping the frequency of the bias signal ω_{bias} while keeping a constant offset frequency of $\Delta\omega/2\pi = 25$ kHz. As a result, the high frequency

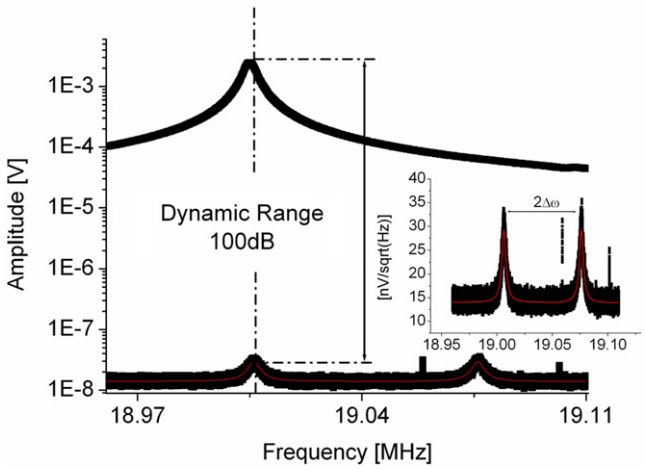

Figure 4. Signal to noise ratio obtained for $V_{\mathrm{drive}} = 1.5$ V and $V_{\mathrm{bias}} = 1.5$ V—noise is computed for 1 Hz bandwidth; the inset corresponds to the noise density peaks around the resonance frequency.

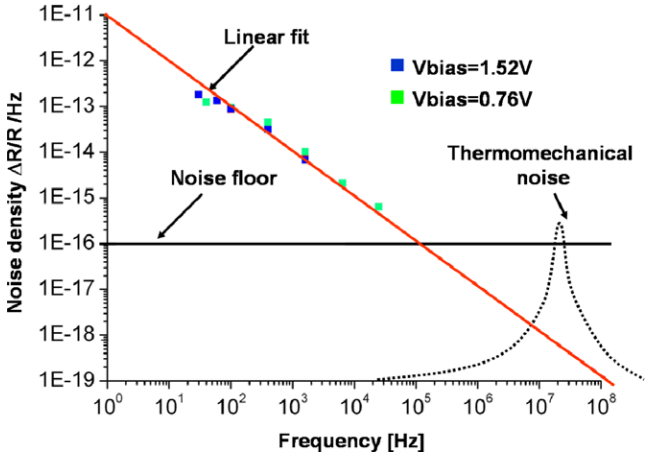

Figure 5. Contribution of different noise sources expressed as relative resistance change, which is independent of V_{bias}. $1/f$ noise density measurement for different bias voltages (colored squares) compared with both the noise floor and the thermomechanical noise. The red curve is the linear fit of the experimental data for $1/f$ noise. The black curve corresponds to the noise floor (i.e. electronic and Johnson noises). The black dashed curve corresponds to a schematic of the thermomechanical noise.

thermomechanical noise was mixed down to a lower frequency $|\omega_{\mathrm{bias}} - \omega_0| = \Delta\omega$. We thus obtained two peaks with amplitudes of 28 nV Hz$^{-1/2}$, separated by 50 kHz (see the inset of figure 4). The noise level is evaluated over a 1 Hz bandwidth.

The noise floor $S_{\mathrm{d}}^{1/2} \approx 13$ nV Hz$^{-1/2}$ resulted from both the Johnson noise and the input noise of the detection electronics. The thermomechanical noise $S_{\mathrm{th}}^{1/2}$ can be calculated from the peak amplitude and the floor level and is approximately 24.8 nV Hz$^{-1/2}$. The Johnson noise is given by $S_{\mathrm{J}}^{1/2} = \sqrt{4k_{\mathrm{B}}TR} \approx 11.2$ nV Hz$^{-1/2}$ ($R \sim 7600\ \Omega$). The electronics noise is then $S_V^{1/2} = \sqrt{S_{\mathrm{d}} - S_{\mathrm{J}}} \approx 6$ nV Hz$^{-1/2}$, which agrees with the noise level specified by the manufacturer of the lock-in amplifier.

Typically, $1/f$ noise created by resistance fluctuations is the main limitation in piezoresistive sensors [9]. However, these resistance fluctuations were not observed in our devices at 20 MHz operating frequency. In order to investigate the consistency of such a result, we computed $1/f$ noise density using Hooge's empirical relation [21],

$$S_{\mathrm{H}} = \frac{H V_{\mathrm{bias}}^2}{N|f - f_{\mathrm{bias}}|}, \tag{6}$$

where N is the total number of carriers within the gauge and f_{bias} is the bias frequency. The Hooge parameter H is extracted from the measurement of the relative resistance variation according to the readout voltage frequency for two amplitudes (see figure 5). An AC bias (∼15 kHz) is used to remove the $1/f$ noise of the lock-in. By linearly fitting the data, we find H to be approximately 10^{-6}. From equation (6), we then estimate the resulting noise to be a few nV Hz$^{-1/2}$ at 20 MHz, which is negligible compared to other sources of noise. To illustrate this, we included the noise floor level (Johnson and electronics noises) and the thermomechanical noise level in terms of relative resistance fluctuation in figure 5. For frequencies higher than 100 kHz, the $1/f$ noise appears to be lower than other noises. This result is in particular obtained thanks to homogeneous doping (10^{19} cm^{-3}) through the whole thickness and specific annealing. A bad doping process in conjunction with a low doping level could lead to the opposite conclusion.

It is important to note that we obtain *a priori* an unexpectedly large SNR (see figure 4). For our semiconductor nanowire gauges, we infer the piezoresistive gauge factor γ to be approximately 40, compared to at most a few units for metallic layer piezoresistors. The large resistance of the gauges is roughly one or two orders of magnitude (∼1 kΩ) larger than that of metallic layer piezoresistors (∼10 Ω). Taking into account the Johnson noise only, the SNR is given by

$$\mathrm{SNR_J} = \frac{V_{\mathrm{out}}}{\sqrt{S_{\mathrm{J}}}} \propto \frac{\gamma V_{\mathrm{b}} \varepsilon}{\sqrt{4k_{\mathrm{B}}TR}} \tag{7}$$

where T and R are the temperature and the gauge resistance respectively, k_{B} is the Boltzmann constant, V_{b} is the RMS value of the bias voltage. V_{out} is proportional to $\delta R/R$ according to equation (3). The SNR for the semiconducting gauge over the SNR of the metallic gauge can be simply expressed by

$$\frac{\mathrm{SNR_{JS}}}{\mathrm{SNR_{JM}}} = \frac{\gamma_{\mathrm{S}} V_{\mathrm{bS}}}{\gamma_{\mathrm{M}} V_{\mathrm{bM}}} \sqrt{\frac{R_{\mathrm{M}}}{R_{\mathrm{S}}}}. \tag{8}$$

Indexes S and M are for the semiconductor gauge and metallic layer respectively.

At constant temperature, considering the aforementioned resistances, V_{bS} can be 100 times larger than V_{bM} because of the respective fusion temperatures of silicon and metals. The $\mathrm{SNR_{JS}}$ is then 10 times larger than $\mathrm{SNR_{JM}}$. The gauge factors of silicon nanowires are much higher than the metallic layer gauges used as piezoresistive detection schemes for NEMS. The signal improvement is then much higher than the noise enhancement and the Johnson noise impact is limited.

3.3. Allan deviation

Usually NEMS is embedded in a phase locked loop (PLL) or a self-excited loop in order to monitor the time evolution of their resonant frequency. The frequency stability of the overall system (e.g. of the NEMS and the supporting electronics) is characterized by the Allan deviation, defined as [9]

$$\delta\omega_0/\omega_0 = \sqrt{\frac{1}{(N-1)}\sum_{1}^{N}\left(\frac{\bar{\omega}_{i+1}-\bar{\omega}_i}{\omega_0}\right)^2} \qquad (9)$$

where $\bar{\omega}_i$ is the average angular frequency in the ith time interval τ, and N is the number of independent frequency measurements, which is assumed to be a sufficiently large number. The mass resolution δm is then $\sqrt{2}M_{\text{eff}}\delta\omega_0/\omega_0$ for 1 s integration time. The theoretical Allan deviation can be expressed as [6]

$$(\delta\omega_0/\omega_0)_{\text{th}} = 10^{-\text{DR}/20}/\sqrt{2}Q. \qquad (10)$$

For the experimental dynamic range (DR) of 100 dB (see figure 4) the ultimate Allan deviation would be around 1.5×10^{-9} over a 1 s integration time. For an effective mass of 140 fg (see table 2) and a Q-factor of 5000, this would result in a potential mass resolution of $\delta m = \frac{M_{\text{eff}}}{Q} \times 10^{-(\text{DR}/20)} \approx$ 0.3 zg at room temperature and at relatively low frequency (20 MHz). As mentioned afterward, this theoretical mass resolution should be considered as the lower limit.

The experimental Allan deviation was measured in open loop recording of the phase variation of the electrical signal at the NEMS output. The NEMS was driven at its resonant frequency (20 MHz). The Allan deviation was measured in three steps (for short, intermediate and long times). For low time constants (<0.1 s), the integration time of the lock-in and the global acquisition time were 100 μs and 10 s respectively. For larger time constants, they were set to 100 μs and 4000 s (50 000 s) respectively. These adjustments remove the effect of the lock-in filtering that would artificially decrease the Allan deviation and ensure at least 100 points for each interval. We can also note that the smallest interval is set by the transient time Q/f (i.e. ~250 μs in our case). Typical experimental data are shown in figure 6. For mass sensing the study has to be focused on short times lower than 1 s. Typically, we achieved an Allan deviation of 10^{-6} for $\tau = 1$ s at room temperature. For long time constant, the minimum Allan deviation reaches 6×10^{-7}. This value is quite a classical one, reported in many papers (see [3, 9, 22] for example), and might be considered as the experimental limit.

The large difference of three orders of magnitude between the expected value and the experimental Allan variance has to do with the fact that actuation is not present during thermomechanical noise measurement. The DR measurements therefore do not take into account noise contributions from the actuation voltage and the thermal bath. Considering both a typical silicon NEMS temperature coefficient of 50 ppm K^{-1} and an Allan deviation close to 10^{-6}, the related thermal bath temperature fluctuations will be around 10^{-2} K. The effect of temperature fluctuations on cantilever measurements is well explained in [23]. To get better frequency stability we think that the temperature fluctuation should be controlled to at least below this value. It is also essential to suppress the background level as much as possible in order to reduce the additional phase noise that results from background fluctuations associated with electronic and temperature instabilities. The discrepancy between the Allan deviation obtained with equation (10) and the experimental data is an open question that is currently being studied.

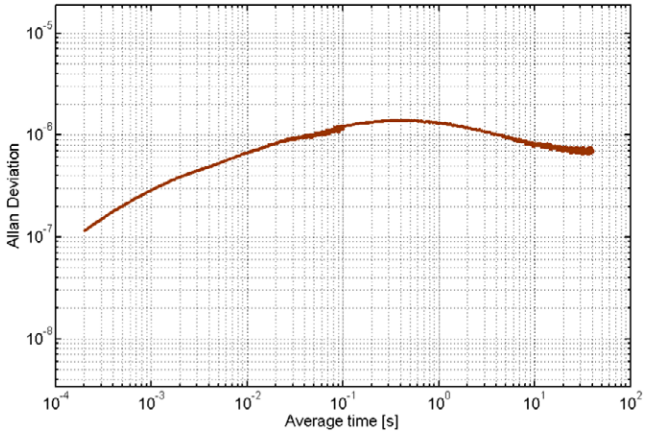

Figure 6. Allan deviation measured in the open loop condition for $V_{\text{drive}} = 1.5$ V and $V_{\text{bias}} = 1.5$ V.

4. Conclusion

In this paper, we demonstrate a new kind of detection scheme based on doped silicon nanowire strain gauges that are fully compatible with CMOS processes. This allows very large scale integration of devices in a straightforward manner. Measurements obtained with this approach are showing promising performances in terms of frequency stability, dynamic range, and achievable mass resolution. The devices tested in this work were developed as prototypes and were not optimized for mass detection at this stage. Such NEMS thus have a great potential for future performance improvements and new applications opportunities. Further device optimization for lower mass and higher frequency, based on advanced top-down nanowire fabrication techniques [24] with expected giant gauge factors, will lead to a resolution in the range of a few zeptograms or less.

Several papers [3, 7, 10] have argued for the importance of reducing the fundamental sources of noise by optimizing the NEMS design. However, a tremendous effort is also needed to study and understand the coupling between NEMS and their environment (temperature fluctuation, packaging), which apparently limits the resolution so far.

This device with the lever arm architecture, symmetric piezoresistive gauges and decoupling between the electrostatic actuation and piezoresistive detection makes the measurements more efficient and the signal over noise ratio higher. Compared to metallic gauges, doped silicon gauges produce a much larger signal thanks to a much higher intrinsic gauge factor and

larger allowed bias voltages (due to their higher resistance). The signal is thus much easier to detect while the noise floor remains very low, as it is dominated by thermomechanical and electronic, rather than Johnson, noise. Flicker noise ($1/f$ noise), which is often cited as a huge barrier for doped silicon based piezoresistive detection, is not an issue for RF resonance frequencies.

The very large scale integration (VLSI) of devices described in this work will enable a wide range of new devices, such as arrays of massively parallel oscillating NEMS, sensitive multigas sensors, and NEMS mass spectrometry with very low frequency dispersion less than 1%.

References

[1] Yang Y T, Callegari C, Feng X L, Ekinci K L and Roukes M L 2006 *Nano Lett.* **6** 583–6
[2] Ilic B, Craighead H G, Krylov S, Senaratne W, Ober C and Neuzil P 2004 *J. Appl. Phys.* **95** 3694
[3] Arcamone J, van den Boogaart M A F, Serra-Graells F, Fraxedas J, Brugger J and P'erez-Murano F 2008 *Nanotechnology* **19** 305302
[4] Jensen K, Kim K and Zettl A 2008 *Nat. Nanotechnol.* **3** 533
[5] Staufer U *et al* 2007 *Microelectron. Eng.* **84** 1681
[6] Ekinci K L, Yang Y T and Roukes M L 2004 *J. Appl. Phys.* **95** 2682
[7] Duraffourg L, Colinet E, Ollier E, Hentz S, Andreucci P, Reig B and Robert P 2008 *Appl. Phys. Lett.* **92** 174106
[8] Colinet E *et al* 2009 *IEEE J. Solid-State Circuits* **44** 247
[9] Feng X L, White C J, Hajimiri A and Roukes M L 2008 *Nat. Nanotechnol.* **3** 342
[10] Li M, Tang H X and Roukes M L 2007 *Nat. Nanotechnol.* **2** 114
[11] Lassagne B, Garcia-Sanchez D, Aguasca A and Bachtold A 2008 *Nano Lett.* **8** 3735
[12] Ayari A, Vincent P, Perisanu S, Choueib M, Gouttenoire V, Bechelany M, Cornu D and Purcell S T 2007 *Nano Lett.* **7** 2252
[13] Colinet E, Duraffourg L, Labarthe S, Robert P, Hentz S and Andreucci P 2009 *J. Appl. Phys.* **105** 124908
[14] He R and Yang P 2006 *Nat. Nanotechnol.* **1** 42
[15] Ollier E *et al* 2007 *IEEE-NEMS-07 (Bangkok, Jan 2007)* pp 180–5
[16] Ju Y, Ju B F and Saka M 2005 *Rev. Sci. Instrum.* **76** 054701
[17] Kanda Y 1982 *IEEE Trans. Electron Devices* **29** 64
[18] Bargatin I, Kozinsky I and Roukes M L 2007 *Appl. Phys. Lett.* **90** 093116
[19] Huttel A K, Steele G A, Witkamp B, Poot M, Kouwenhoven L P and van der Zant H S J 2009 *Nano Lett.* **9** 2547
[20] Ekinci K L, Yang Y T, Huang X M H and Roukes M L 2002 *Appl. Phys. Lett.* **81** 2253
[21] Harley J A and Kenny T W 1999 *Appl. Phys. Lett.* **75** 289
[22] Verd J, Uranga A, Abadal G, Teva J L, Torres F, Lopez J, Perez-Murano F, Esteve J and Barniol N 2008 *IEEE Electron Device Lett.* **29** 146
[23] Giessibl F J 2003 *Rev. Mod. Phys.* **75** 949
[24] Ernst T *et al* 2008 *IEDM 2008: Electron Devices Mtg* (Piscataway, NJ: IEEE)